Journal of Materials Chemistry A

PAPER

View Article Online
View Journal | View Issue

Cite this: J. Mater. Chem. A, 2018, 6, 1513

Expanded biomass-derived hard carbon with ultra-stable performance in sodium-ion batteries†

Ziyi Zhu,[a] Feng Liang,[a] Zhongren Zhou,[a] Xiaoyuan Zeng,[a] Ding Wang,[a] Peng Dong,[a] Jinbao Zhao,[b] Shigang Sun,[b] Yingjie Zhang*[a] and Xue Li*[a]

Received 10th September 2017
Accepted 14th December 2017

DOI: 10.1039/c7ta07951f

rsc.li/materials-a

A hard carbon sheet-like structure has been successfully prepared with a short flow process by simply using cherry petals (CPs) as the raw materials. The sodium storage mechanism in CPs was detected with cyclic voltammetry (CV) and X-ray photoelectron spectroscopy (XPS). Encouragingly, when being assessed as an anode electrode for sodium-ion batteries (SIBs), the CP electrode can provide a high initial reversible capacity of 310.2 mA h g^{-1} with a favorable initial Coulomb efficiency of 67.3%, delivering a high retention rate of 99.3% at 20 mA g^{-1} after 100 cycles. Even at a high current density of 500 mA g^{-1}, the reversible capacity can reach 146.5 mA h g^{-1}, indicating that the high rate performance is excellent as well. Such a preferable performance may be derived from the prepared structures with sufficient mesopores, the presence of nitrogen/oxygen functional groups on the surface and the expanded interlayer distances (~0.44 nm), which enable reversible sodium-ion storage through surface adsorption and sodium intercalation.

Introduction

Limited reserves and uneven distribution of lithium make the production cost for lithium-ion batteries (LIBs) high and it is difficult to meet the huge demand for future energy storage markets; thus the development of new energy storage battery systems is particularly important.[1–3] As an alternative, SIBs have attracted wide attention due to their similar chemical properties to lithium and the natural abundance of sodium resources (2.75% of sodium compared to 0.065% of lithium on Earth).[4]

The key factor in the development and application of SIBs is the high-performance electrode materials. Carbon materials are widely used as capacitor or battery electrode materials due to their low-cost and simple processing.[5,6] However, in the field of SIB research, the radius of a sodium ion (0.102 nm) is much larger than that of a lithium ion (0.076 nm), which makes a limitation for sodium ion transfer during the charge/discharge process, resulting in irreversible sodium ion intercalation for graphite materials.[7,8] The search for an anode with appropriate sodium voltage storage, a large reversible capacity and high structural stability remains an obstacle to the development of SIBs.[9–11] Non-graphite carbon materials as a research hotspot have a large interlayer distance and disordered structure, which are conducive to the insertion/extraction of a sodium ion. According to the degree of graphitization and graphite microcrystalline arrangement, non-graphite carbon materials are mainly divided into soft carbon[12] and hard carbon.[13,14] Compared with soft carbon, hard carbon has larger carbon layer spacing, disorderly micropores and more sodium sites, and is considered to be an ideal SIB anode material with higher storage capacity.[15]

Hard carbon is widely researched. Wenzel *et al.*[16] demonstrated for the first time that nanotechnological strategies can be successfully applied in SIBs. Li *et al.*[17] combined soft carbon with hard carbon to prepare monodispersed hard carbon spherules coated with soft carbon. Jian *et al.*[18] anchored Fe_2O_3 nanocrystals onto graphene nanosheets (Fe_2O_3@GNS) by a nanocasting technique. As a kind of hard carbon, biomass-derived carbon has attracted much attention from experts and scholars due to the characteristics of rich-resource, low-cost and simple preparation process. It can also maintain the natural properties of biomass precursors, which contribute to the improvement of electrochemical performance. Cao *et al.*[19] prepared hard carbon from rapeseed seeds with an interlayer distance of 0.39 nm, delivering a capacity of 237 mA h g^{-1} at 25 mA g^{-1}. Hong *et al.*[20] prepared a porous hard carbon material by the simple pyrolysis of H_3PO_4-treated pomelo peels with a reversible capacity of 71 mA h g^{-1} at 5000 mA g^{-1} and a capacity of 181 mA h g^{-1} after 220 cycles at 200 mA g^{-1}, but the initial Coulomb efficiency was only 27%. In addition, peanut

[a]National and Local Joint Engineering Laboratory for Lithium-ion Batteries and Materials Fabrication Technology, Yunnan Provincial Laboratory for Advanced Materials and Batteries Application, Faculty of Metallurgical and Energy Engineering, Kunming University of Science and Technology, Kunming 650093, Yunnan, China. E-mail: zyjkmust@126.com; 438616074@qq.com

[b]State Key Laboratory of Physical Chemistry of Solid Surfaces, Collaborative Innovation Center of Chemistry for Energy Materials, College of Chemistry and Chemical Engineering, Xiamen University, Xiamen, 361005, Fujian, China

† Electronic supplementary information (ESI) available. See DOI: 10.1039/c7ta07951f

skin,[21] banana peels,[22] apple biowaste,[23] and natural leaves[24] have also been confirmed to prepare hard carbon.

Although previous studies demonstrate the feasibility of biomass-derived carbon materials, there are still two major challenges: first, the initial Coulomb efficiency of the material is low due to the formation of a solid electrolyte interface (SEI) film; second, the degree of graphitization of the material is not high, which usually makes its cycle and magnification performance non-ideal. In the present work, cherry petals were used as precursors to prepare hard carbon with an expanded interlayer distance of 0.44 nm by a facile preparation. When used as an anode material for SIBs, the CPs exhibit high storage capacity with a high initial reversible capacity (310.2 mA h g^{-1}), outstanding cyclic stability (the capacity retention rate was 99.3% after 100 cycles at 20 mA g^{-1}), favorable rate capability (146.5 mA h g^{-1}, even at a very high current density of 500 mA g^{-1}) and a high initial Coulomb efficiency of 67.3%. In particular, approximately 45% of the capacity from the CP is contributed by sodiation below 0.1 V (*vs.* Na^+/Na). This low potential plateau makes the CP energetically favorable as an anode material. The excellent electrochemical properties of the CP can be attributed to its "open" lamellar structure-associated nanoscale mesopores, the presence of nitrogen/oxygen functional groups on the surface, and the expanded interlayer distance (~0.44 nm). In addition, the electrochemical process is also researched by CV and XPS analysis.

The sodium storage mechanism of hard carbon is controversial as reported and there are two main viewpoints.[13,25] (I) "Intercalation–adsorption" mechanism: the capacity of the high potential slope region is mainly derived from sodium-ion insertion into graphite sheets, and the low potential platform region corresponds to adsorption of sodium in defected sites, edges, and the surface of nanographitic domains. (II) "Adsorption–intercalation" mechanism: the capacity of the high potential slope region is mainly due to the adsorption of sodium in defected sites, edges, and the surface of nanographitic domains. The low potential platform region is derived from sodium-ion insertion into the graphite sheets. In our work, we detected that the possible sodium-ion insertion of the CP belongs to the "adsorption–intercalation" mechanism. Generally speaking, this work combines the unique morphology and structure of biomass precursors with simple processing techniques to obtain a promising carbon material with low cost and excellent electrochemical performance.

Experimental

Materials synthesis

CPs were prepared using the hydrolyzate of cherry petals treated with dilute hydrochloric acid. First, the collected cherry petals were washed and dried at 80 °C to remove water. Then the cherry petals were placed in a tube furnace and carbonized at 1000 °C for 1 h under Ar flow with a ramping rate of 10 °C min^{-1}. After that, the obtained black powder was immersed in dilute hydrochloric acid to remove the inorganic impurities formed on the surface, and finally, washed with deionized water and dried at 80 °C.

Materials characterization

Thermogravimetric analysis data were obtained by heating from room temperature to 1000 °C under Ar flow with a ramping rate of 10 °C min^{-1} by thermogravimetric analysis (NETZSCH STA 449F3, Germany). The composition of the surface functional groups before and after carbonization was examined by Fourier transform infrared spectrometry (Bruker TENSOR27, Germany). The morphologies of the samples were observed using scanning electron microscopy (QUANTA FEG 250, America). Structural characterization was performed using X-ray diffraction (Minflex 600, Japan) and Raman spectroscopy (LabRAM HR Evolution, France). Nitrogen adsorption/desorption isotherms were acquired at 77 K using a surface area and pore size analyser (Micromeritics Tristar 3000, America). Specific surface areas were calculated based on the Brunauer–Emmett–Teller method. The Barrett–Joyner–Halenda pore size distribution was determined from the adsorption isotherms. The structural features were determined by high-resolution transmission electron microscopy and selected area electron diffraction (Tecnai G^2 TF30 S-Twin, Netherlands). The chemical state of the surface elements of the material was obtained by X-ray photoelectron spectroscopy (PHI5000 Versaprobe-II, Japan) with a monochromatic Al Kα X-ray source.

Electrochemical measurements

Electrochemical performances of the CP were measured with 2016 coin cells. A slurry of 80% CP, 10% Super-P (conductive agent), and 10% carboxymethyl cellulose (binder) in deionized water was coated onto copper foil, and then dried at 120 °C overnight under vacuum. After that, a roll press for the tabletting treatment was used, allowing the electrode material and collector to be closer together, and improving the flatness of the electrode sheet. All the operations were performed in an argon-filled glove box and both the moisture and oxygen amounts were controlled to be less than 0.5 ppm. Sodium metal was used as the counter electrode and glass fiber was used as the separator. The electrolyte was a solution of 1 M $NaClO_4$ in a solvent mixture of propylene carbonate (PC) with 5 wt% fluoroethylene carbonate (FEC) additive. CV and EIS were measured using an Autolab electrochemical workstation (PGSTAT302N, Switzerland). The discharge/charge tests were carried out on a land battery measurement system (CT2001A, China) over a voltage range of 0.01–3 V (*vs.* Na^+/Na) at various current densities. All of the above electrochemical tests were conducted at room temperature.

Results and discussion

In this work, cherry petals were used as precursors, and they were converted into carbon material by high temperature calcination and immersed in acid to remove impurities. The synthetic route is shown in Fig. 1. Thermogravimetric analysis (TGA) and Fourier transform infrared spectroscopy (FTIR) were used to determine the pyrolysis weight loss characteristics and product formation characteristics of the CP, which provide the theoretical basis for utilization. As illustrated in Fig. S1a,† the

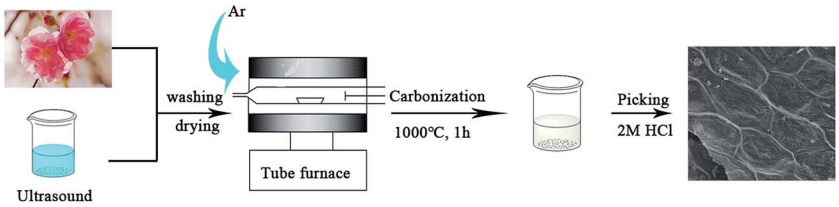

Fig. 1 Preparation scheme of the CP.

thermogravimetric process of the CP is similar to that of other biochar materials, and could be divided into three stages according to the heating process area.[19,26] In the first stage between room temperature and 180 °C, the weight loss is mainly due to the beginning of the thermal degradation phenomenon, and a small amount of moisture adsorbed on the surface of the material evaporates with the elevated temperature. In the second stage from 180 °C to 450 °C, the sharp decline in weight may belong to the loss of volatile organic compounds and the corresponding rapid degradation of carbohydrates and lipids. The chemical composition of the biomass changes significantly, which is the main weight loss stage.[19] As the temperature rises, the weight loss of the pyrolysis substances begins to slow down, which accounts for the carbonization process. The third stage (450 °C to 1000 °C) reveals the migration of volatile components shifting from deep layers to outer layers with a longer process due to the dehydrogenation reaction and the residue is ash and fixed carbon.

FTIR spectra of the precursor and CP are shown in Fig. S1b.† The absorption peak at approximately 3420 cm^{-1} may be assigned to the absorption peak of [–OH] vibrations such as alcohols, phenols and carboxylic acids. However, from the peak value of [–OH], it can be seen that the wave number is not above 3600 cm^{-1}, and the relative position is low, which is due it being affected by the hydrogen bond. There are several smaller peaks in the range of 3000 to 2800 cm^{-1}, which are formed from the [C–H] of aliphatic compounds. [C═C], [C═O], [C–O] and hydrogen atoms outside the aromatic nucleus are formed in the range of 1800 to 800 cm^{-1}. Finally, there is a relatively wide and strong peak in the range of 600 cm^{-1} that may be from amide or phosphorus-containing groups. Compared with the precursors, the content of each functional group is less or even absent for the CP, which means that the O–H bond, C–H bond and C–O bond between the molecules are broken in the pyrolysis process, and a lot of CO, CO_2, CH_4, C_2H_4 and C_2H_6 is generated. This is well consistent with the TGA data, and it can be inferred that this process occurs mainly in the second stage of TGA.

The morphology of the CP was observed by scanning electron microscopy (SEM). As summarized in Fig. 2a, the processed CP maintained the sheet structure of the precursor, indicating that the machined precursor is not only successfully converted to the carbon material but also maintains the original morphology. Observed at a large magnification, it can be seen that the CP surface is composed of uniform "honeycomb" regions of uniform size (Fig. 2b). Fig. 2c shows the magnifyied "honeycomb" area with heterogeneous folds. In addition, it can be seen in Fig. 2d that the pleated surface is very smooth and the amount of pores is less, which would result in a low specific surface area of the large-sized form of CP; this will be analyzed by nitrogen adsorption/desorption isotherms for further verification.

The microstructures of the CP were characterized by X-ray diffraction (XRD) and Raman spectroscopy (Raman). As summarized in Fig. 3a, the XRD pattern shows two weak broad diffraction peaks at 2θ ~22° and ~43°, corresponding to the diffraction of (002) and (101) planes, indicating that the CP is a typical nonlinear carbon material with a highly disordered structure.[27] The calculated thickness of the graphite microcrystalline layer along the *c*-axis direction (L_c) is 1.13 nm. On the other hand, the empirical parameter *R* calculated as the ratio of the (002) peak height to the background height is 2.62, indicating that the CP is composed of disordered graphite microcrystallites with a small amount of stacked-graphite sheets.[28] In addition, according to the previous studies on biomass derived carbon materials, the storage of the sodium ion is affected by the degree of graphitization for the material.[22] Raman spectroscopy was used to research the degree of graphitization for the CP. Fig. 3b shows that there were two separate characteristic bands of the D-band peak (defect inducing band) at ~1343 cm^{-1} and the G-band peak (crystalline graphite band) at ~1589 cm^{-1}, which are two intrinsic peaks for carbon materials.[27] The intensity ratio of the D-band over the G-band (I_D/I_G) of the CP is 1.02, and the smaller value indicates that the CP has a higher degree of graphitization. Moreover, the value of I_D/I_G can be used to calculate the crystallite width in the *a*-axis

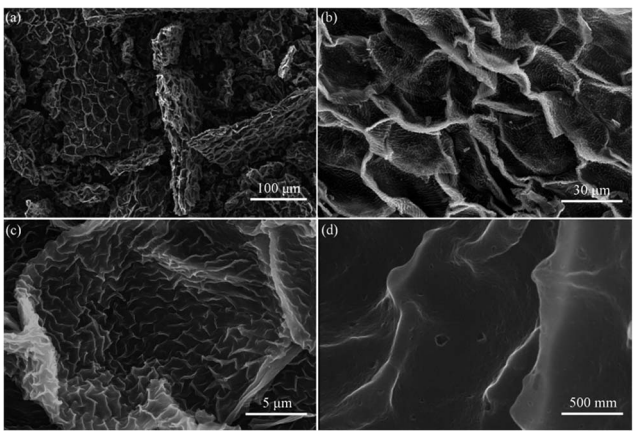

Fig. 2 Different magnification SEM images of the CP.

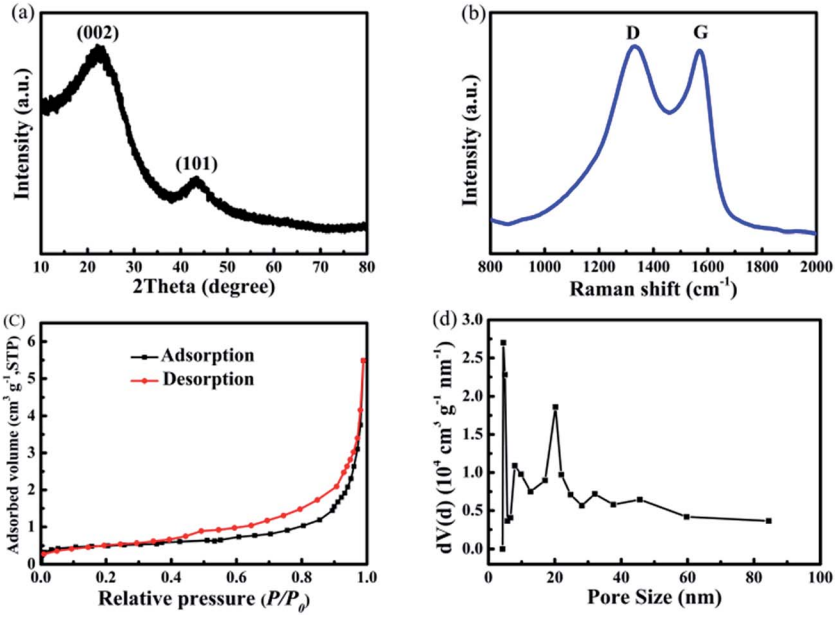

Fig. 3 (a) XRD pattern and (b) Raman spectrum of the CP; (c) nitrogen adsorption/desorption isotherms and (d) BJH pore size distributions of the CP.

direction (L_a) as 3.86 nm, and the smaller crystallite size shortens the transmission distance of the sodium ion.

Fig. 3c shows the nitrogen adsorption/desorption isotherms of the CP, which are typical IV isotherms. It can be deduced that the mesoporous distribution of CP particles is mainly caused by the volatilization of gas in the carbonization process.[29,30] At the same time, there is a significant H3-type hysteresis loop at a relative pressure (P/P_0) between 0.4 and 1.0, indicating that the CP is a sheet-like granular material, which is well consistent with the observed results of the TEM images. The pressure zone was observed not to show adsorption saturation, indicating that the pore structure is irregular. The pore structure of the CP was calculated using the Barrett–Joyner–Halenda (BJH) model. As shown in Fig. 3d, the data of the adsorption branch were observed in order to avoid the occurrence of false peaks. Brunauer–Emmett–Teller (BET) analysis shows that the specific surface area of the CP is 1.86 $m^2 g^{-1}$ and the average pore size is 4.49 nm. As we know, the lower specific surface area can inhibit the formation of the SEI film, thereby increasing the initial Coulomb efficiency of the carbon-based anode material for SIBs, while the nanoscale mesopores are considered to contribute to the storage of the sodium ion.[20,31]

The microstructure of the CP was studied in detail by high-resolution transmission electron microscopy (HRTEM) and selected area electron diffraction (SAED). As summarized in Fig. 4a, the CP consists of random and disordered graphite microcrystals, in which the layered structures are well resolved by alternating bright and dark contrast, indicating that the CP is a very typical hard carbon structure. In theory, hard carbon has a variety of sodium storage forms, so the reversible specific capacity is higher.[15] The highly disordered microstructure could also be shown by the SAED pattern with an electron diffraction ring; the diffraction spots do not appear in the dispersed diffraction ring, further illustrating the properties of hard carbon for the CP. In addition, the progressive change in the interlayer distance is also clearly apparent. The contrast line profiles across a small amount of graphite microcrystals stacked at representative locations, indicated by arrows, are plotted under the corresponding images, as shown in Fig. 4b. The average interlayer distance is measured to be ~0.44 nm for the CP, which is much larger than that of graphite (0.335 nm).[32] The expanded interlayer distance is not only beneficial to the insertion/extraction of the sodium ion, increasing the storage capacity of sodium ions in the CP, but also maintains the stability of the material structure during the charge/discharge cycle and improves the cycle performance of the CP. The results of HRTEM and SAED are well consistent with the results detected by XRD and Raman patterns.

XPS was used to determine the elements contained on the surface of the CP and the corresponding chemical states. Fig. S2a† shows the full spectrum of the CP, showing the apparent spectral regions of C 1s and O 1s. Table S1† gives the percentages of the elements. As shown in Fig. S2b,† three peaks are obtained in the XPS spectrum of the C 1s region, and the peak area ratio at 284.6 eV was 48.6%, corresponding to the C–C bond in the defect-free graphite lattice. The C–O and C=O bonds of the defective graphite lattice are located at 285.9 and 288.9 eV with a peak area ratio of 11.2% and 40.2%, respectively. It is worth noting that no peak representing the π–π interaction is detected in C 1s region of the XPS spectrum of the CP, and it is further verified that the CP is stacked by a smaller graphite sheet from XRD analysis. The XPS spectra of O 1s show two sub-peaks (Fig. S2c†), belonging to the C=O bond and the C–OH bond of 530.3 and 532.5 eV, respectively.[33–35] These oxygen-containing functional groups could participate in the surface oxidation–reduction reaction of the sodium ion (*i.e.*, C=O +

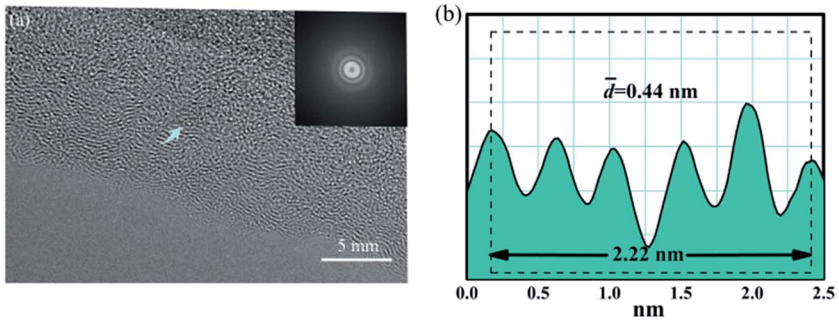

Fig. 4 (a) HRTEM and SAED images of the CP; (b) contrast profiles along the arrows indicate the interlayer distance of the CP.

$Na^+ + e^- \rightarrow$ –C–O–Na), which could further enhance the sodium ion storage capacity of the CP.[36] In addition, the nitrogen content of the CP surface is relatively high and the presence of nitrogen/oxygen functional groups can support the sodium ion stored defect sites.[36]

Fig. 5a shows the CV curves of the CP in the range of 0.01–3 V (*vs.* Na^+/Na) at a scan rate of 0.1 mV s^{-1}. The area enclosed by the CV curve represents the total amount of stored charge generated by faradaic and non-faradaic reaction processes. In the first reduction process, the reduction current peak observed near 1.15 V is due to the reaction between the sodium ion and the functional groups on the surface of the CP, behaviour that was reported previously for lithium storage mechanisms of carbonaceous materials.[37] As it is known that the decomposition voltage of PC is 0.7 V in LIBs,[38,39] considering the standard electrode potential difference ($E^0(Li^+/Li) - E^0(Na^+/Na) = -0.33$

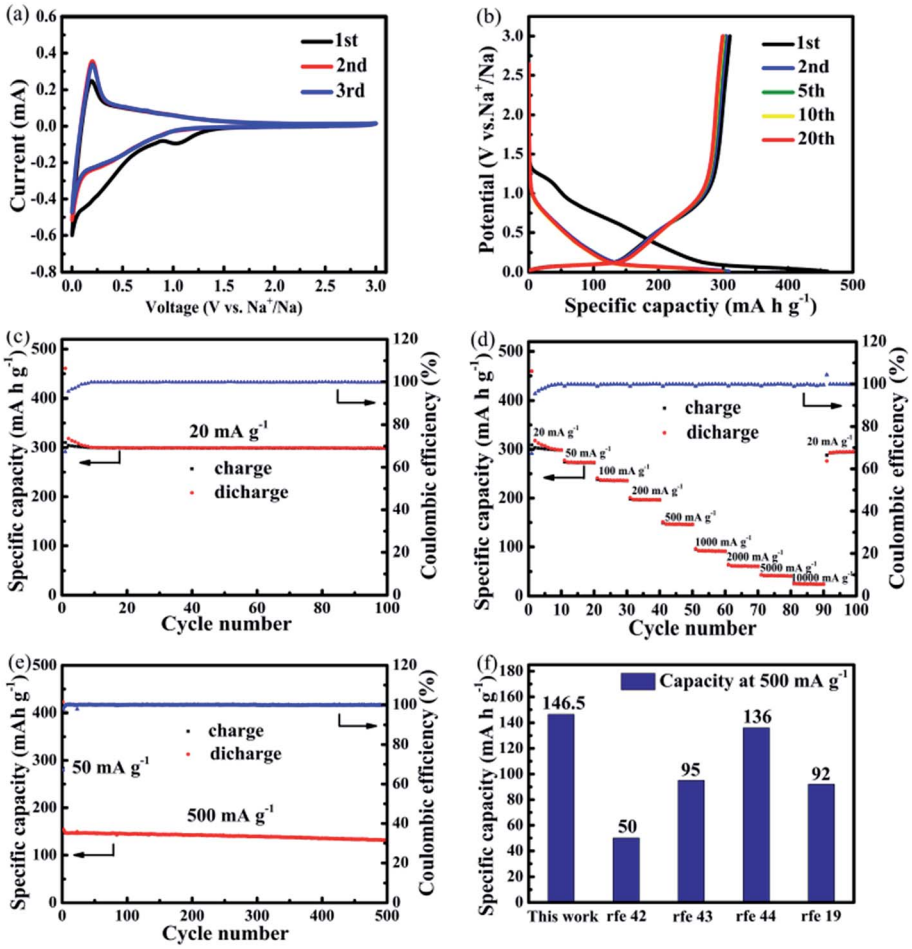

Fig. 5 Electrochemical performance of the CP: (a) CV curves; (b) galvanostatic charge/discharge cycling profiles; (c) cycling performance (at 20 mA g^{-1}); (d) rate performance; (e) long-term cycling performance (at 50 mA g^{-1} in the first cycle and at 500 mA g^{-1} in subsequent cycles); (f) rate performance comparison of the CP with the state-of-the-art materials from the literature.

V), the reduction current peak observed near 0.25 V corresponds to the PC decomposition and formation of SEI film on the surface of the carbon crystal. Tang *et al.*[40] reported a similar result that PC decomposes at 0.26 V in SIBs with a reduced graphene oxide anode. These two reduction peaks disappear during the subsequent two cycles, which means that the irreversible reaction of the SEI film and the side reaction of the surface functional groups occur mainly during the first cycle, explaining why the initial Coulomb efficiency of the CP is low. Simultaneously, a pair of sharp redox peaks appears at the low potential region near 0.01 V, which corresponds to the insertion/extraction of the sodium ion in hard carbon, similar to graphite materials. Furthermore, a pair of weak redox peaks is observed at the potential region of 0.1 to 1.6 V, which can be ascribed to the adsorption behavior of the sodium ion on the carbon surface. The mechanism of sodium storage will be further researched in later studies. However, in addition to the first cycle of reversible capacity loss, the subsequent cycles of CV curves can overlap well, which illustrates the excellent stability of sodium ion insertion/extraction during the subsequent cycles.

The galvanostatic charge/discharge cycling profiles of the CP electrode were measured in the potential range of 0.01–3 V (*vs.* Na^+/Na) at a constant current rate of 20 mA g^{-1} as shown in Fig. 5b. Similar to hard carbon as an anode electrode for LIBs, the charge/discharge curves of the CP appear as U-shaped and V-shaped patterns, which express the high potential slope region and the low potential platform region.[41] Consistent with the CV results, the high potential slope region of 1.2 to 0.1 V in the discharge curve refers to the adsorption behavior of the sodium ion on the surface of the material and the low potential platform region below 0.1 V corresponds to sodium ion insertion/extraction in the interlayer of the graphitic microcrystallites. During the charging process, the slope region from 0.1 to 1.2 V is characteristic of the sodium ion removal process. In addition, the prepared CP electrode has a large discharge specific capacity of 461.1 mA h g^{-1} and a charge capacity of 310.2 mA h g^{-1} in the initial cycle with a high initial Coulomb efficiency of approximate 67.3%. Compared with the literature, it can be seen that the CP has a higher initial Coulomb efficiency, which is mainly due to the low specific surface area of the CP causing stable SEI film formation. In the subsequent cycles, the charge/discharge curves surrounding the area of the CP are very small from the second to the twentieth cycles, further illustrating the high cycle stability of the CP electrode. In a word, there are two main sources of irreversible capacity for the CP: first, the generated SEI film makes it so that the embedded part of the sodium ion cannot be properly removed. Second, most of the sodium ions are consumed by reacting with the functional groups on the surface of the CP.

Fig. 5c shows the cycle characteristic curves and the related Coulomb efficiency of the CP. The CP electrode delivers a capacity of 300.2 mA h g^{-1} at 200 mA g^{-1}, and even has a reversible capacity of 298.1 mA h g^{-1} after 100 cycles, with an ultra-high retention rate of approximately 99.3%, indicating a stable cycling performance. With the increase of the number of cycles, the Coulomb efficiency gradually becomes increased and stabilized, indicating that the SEI film is mainly formed in the initial deposition process, similar to the CV results. As shown in Fig. 5d, this electrode presents initial reversible capacities of 298.7, 273.1, 236.5, 196.7, 146.7, 91.9, 61.5, 41.7 and 25 mA h g^{-1} at current rates of 20, 50, 100, 200, 500, 1000, 2000, 5000 and 10 000 mA g^{-1}, respectively. It is worth noting that when the current density decreased back to 20 mA g^{-1}, the discharge capacity of the CP is restored to 292.5 mA h g^{-1} and maintained 97.9% of the initial value, which indicates that the CP electrode exhibits a high rate capability and structural stability even at very high sodium ion insertion/extraction velocities. We believe this is mainly due to the expanded interlayer distance, which is conducive to sodium ion transmission, thereby enhancing its rate performance. The galvanostatic charge/discharge cycling profiles of the CP electrode at different current rates (from 20 to 10 000 mA g^{-1}) are depicted in Fig. S3a.† The decreased reversible capacity during the high current cycling is clearly caused by the shortening of the low potential platform region. The plateau shifts below the lower cutoff potential at elevated current densities, which is attributed to the increasing ohmic drop.

In order to further study the cycling performance of the CP electrode under high current density, we used a low current density of 50 mA g^{-1} for the first charge/discharge process, and a high current density of 500 mA g^{-1} for the next cycles. As can be seen in Fig. 5e, a capacity of 131.5 mA h g^{-1} can be obtained after 500 cycles at a high current density of 500 mA g^{-1} with a retention rate of 89.8%. The galvanostatic charge/discharge cycling profiles are also shown in Fig. S3b.† The CP electrode demonstrates good cycling performance even at high current densities. Fig. 5f illustrates the rate performance comparison for the CP and other hard carbons, and the electrochemical performance of the CP is still prominent even at a high rate.

The SEM image of the CP electrode after 100 cycles at a current density of 20 mA g^{-1} was also investigated. As shown in Fig. S4,† the surface of the electrode after 100 cycles is relatively rough, which can be attributed to the formation of a dense and stable SEI film on the surface of the electrode during cycling, consistent with CV curve analysis, and research on the SEI film will be conducted in detailed analysis below. It is worth noting that the stable SEI film favors the cycling performance of the CP electrode.

Comparing the CP with newly reported hard carbons in Table S2,†[19–21,25,27,42–54] it can be found that the initial Coulomb efficiency, reversible capacity and cycling performance of the CP electrode are excellent. The superior properties of the CP electrode can be attributed to the synergistic effect of sheet morphology with low specific surface area, which has nanosized mesopores, special nitrogen/oxygen functional groups on the surface, and expanded interlayer distance. First of all, the low specific surface area makes the generated SEI film stable, greatly enhancing the initial Coulomb efficiency of the material. Secondly, the distribution of mesopores is not only beneficial to the efficient transport of the sodium ion, but also shortens the diffusion path for the sodium ion. Thirdly, the presence of nitrogen/oxygen functional groups on the surface of the material increases the defective sites that partially improve the

storage of the sodium ion, which contributes to the adsorption of the sodium ion on the surface of the material. Fourthly, the larger interlayer distance contributes to the diffusion and storage of the sodium ion into the graphite sheets and does not destroy the structure of the material, which is critical to the electrochemical properties of the material. Finally, it is certain that the "open" flake structure also serves to reduce the diffusion time of the sodium ion.

In order to further understand the charge transfer kinetics of the materials, electrochemical impedance spectra (EIS) were obtained for the CP electrode. Fig. 6a shows the impedance spectra of the battery under test conditions of 10^5–10^{-2} Hz and 1 mV s^{-1}. The Nyquist curve is composed of the medium–high frequency region for the semicircle and the low frequency region for the straight line, and the equivalent circuit model was fitted in Fig. 6b. The semicircle can be expressed as an ohmic contact resistance (R_s), including the intrinsic resistance of the electrolyte and the active material, and the contact resistance at the electrode/electrolyte interface. In addition, the semicircle is also caused by the charge transfer between the electrode and the electrolyte, corresponding to the charge transfer impedance (R_{ct}). This process could be represented by the R_{ct}/CPE parallel circuit, where CPE is an electric double layer capacitor. It is noteworthy that in the high frequency region from the first cycle to the 200th cycle, the formation of the SEI film during the charge/discharge process will increase the diffusion resistance of the sodium ion through the SEI film on the surface of the material (R_{SEI}), and this process can be representative as the R_{SEI}/CPE parallel circuit. The oblique line in the low frequency region represents the Warburg impedance (Z_w),[55,56] which is caused by the ion during the diffusion process. In addition, the fitting EIS data according to the equivalent circuit are shown in Fig. 6b, and the error between the test data is within 5% (Table S3†), which indicates the right analog circuits. As shown in Table S3,† R_s increases significantly as the number of cycles increases, while the increase in $R_{ct} + R_{SEI}$ gradually decreases, indicating that most of the SEI film is formed during the first cycle and remains stable in subsequent cycles. Thus, the formation of the SEI film would reduce the storage of the sodium ion induced by the active site, resulting in a loss of reversible capacity.

CV is also an effective method to characterize the electrochemical reaction mechanism. It is to be understood that there is a relationship between the peak current and the scanning rate:[57]

$$i = av^b$$

where a and b are constants associated with the reaction mechanism. In particular, a b-value of 0.5 would indicate that the current is controlled by semi-infinite linear diffusion, such as intercalation; a value of 1 indicates that the current is surface-controlled, *i.e.* adsorption. CV curves of the CP electrodes were obtained at scan rates between 0.05 and 1 mV s^{-1} as shown in Fig. 7a. As the scanning rate decreases, the total stored charge of the electrode material increases, which may be due to the limited diffusion of the sodium ion during rapid scanning, and the sodium ion cannot be fully involved in the reaction, resulting in a decrease in the total charge produced by the reaction.[58] Similarly, the increase of the scanning rate causes the oxidation peaks of the electrode material to move in a positive direction, and the reduction peaks to move in a negative direction. The potential difference value ($\Delta E = |E_O - E_R|$) of the oxidation peak potential (E_O) and the reduction peak potential (E_R) increases, which is due to the polarization of the electrode. The ΔE value of the electrode material is more than 59 mV, indicating that the redox is a quasi-reversible process. As shown in Fig. 7b, it is found that the logarithm of the peak current value of the low potential platform region ($\log i_p$) and the logarithm of the sweep rate ($\log v$) satisfy the linear regression ($R^2 = 0.9997$). It can be concluded that the redox reaction process of the CP in the low voltage region is controlled by semi-infinite linear diffusion,[27,31,56] represented by the intercalation of the sodium ion. It is shown that the high potential slope region corresponds to the adsorption of sodium in defected sites, edges, and the surface of nanographitic domains. Meanwhile, the low potential platform region belongs to the insertion of the sodium ion in the graphite sheets. All of the above results reveal that the sodium storage mechanism of the CP electrode follows the "adsorption–intercalation" process.

XPS was used to reveal the surface reaction mechanism of the CP electrode. The Na 1s spectral region of the CP electrode during the charge/discharge process is shown in Fig. 8a. Combined with the CV data, we selected eleven electrochemical response points in the charge/discharge process for a detailed analysis. The Na 1s spectra do not completely disappear after

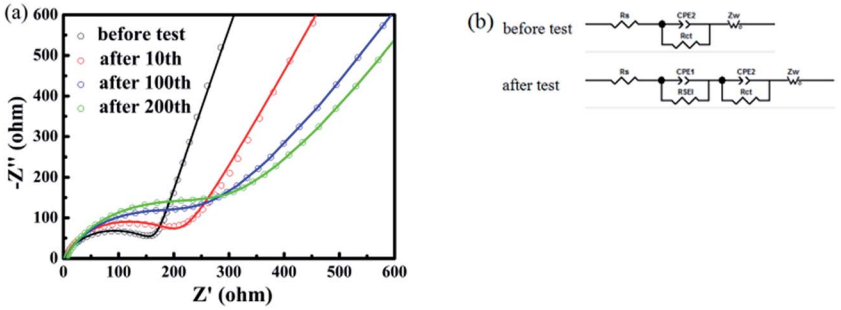

Fig. 6 (a) Electrochemical impedance spectra of the CP electrodes before and after the 10th, 100th, and 200th cycle; (b) equivalent circuits used for fitting the experimental data before and after different cycle numbers.

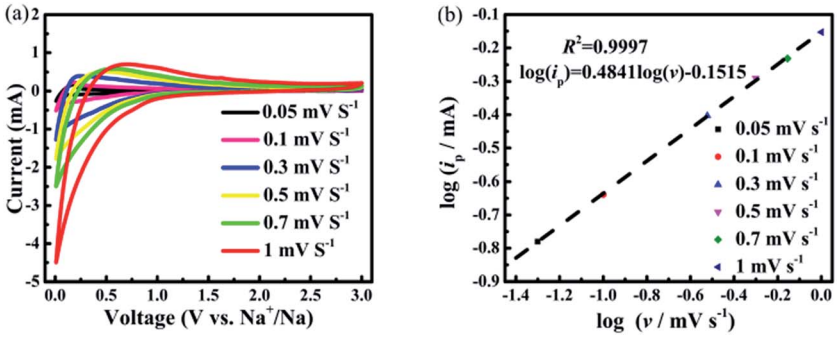

Fig. 7 (a) CV curves for the CP electrodes between 0.01 and 3.0 V at different scan rates; (b) log(i_p) *versus* log(v).

the first charge/discharge cycle, indicating that there is a partial sodium ion remaining on the surface of the CP electrode, which can explain the irreversible reaction of the SEI film and the side reaction of the surface functional groups during the initial cycling. The Na 1s spectra of the charge and discharge process at 1.6, 1.15, 0.25 and 0.1 V are basically coincident, indicating that the material structure has a favorable reversibility of sodium storage during cycling. Importantly, the binding energy of the Na 1s spectra at a discharge to 0.01 V is 1071.4 eV, which is greater than that of discharge to 0.1 V (1071.2 eV), indicating that the Na 1s spectra are shifted to high binding energy. Na has a significant increase in valence, explaining that the low potential platform region corresponds to sodium ion insertion/extraction in the interlayer of the graphitic microcrystallites. When charged from 0.01 V to 0.1 V, the binding energy of the Na 1s spectra is shifted back to 1071.2 eV again, demonstrating that the sodium ion can be reversibly inserted/extracted between the graphitic microcrystallites, which can be attributed to the expanded interlayer distance. At the same time, either under charge or discharge, the binding energy of the Na 1s spectra from 0.1 V to 3 V is similar, indicating that there is no high state Na production in the high potential slope region. Combined with the CV results above, it is clear that the high potential stage is not controlled by diffusion and shows sodium ion adsorption behavior on the surface of the material.[59]

The C 1s and O 1s spectra were also used to analyze the composition of the SEI film. Fig. 8b shows the C 1s spectra, and the strongest peak at 284.5 eV of the original electrode is assigned to the sp^2 carbon in the C–C bond of graphene of hard carbon, while the other peaks are the various functional groups on the surface of the CP electrode.[20] After cycling, these are also observed on the surface of the electrode. However, the C 1s spectra becomes complicated and some new peaks appear associated with the SEI component, which is due to the partial decomposition of the electrolyte in the presence of the FEC additive.[20,60] These peaks are attributed to various compounds, such as the alkyl carbonate of $ROCO_2Na$ and alkali carbonate of Na_2CO_3 at 290.7 eV, the ester linkage (–CO–O–) at 286.9 eV and $–CH_2–$ at 285.5 eV.[61–63] The decomposition of the electrolyte and the formation of the SEI film can be further proven by the O 1s spectra. As illustrated in Fig. S5a,† the existence of $ROCO_2Na$ and Na_2CO_3 can also be observed, corresponding to the peak at 531.9 eV. The peak with the binding energy of 533.8 eV corresponds to RONa, which is assigned to oxygen in alkoxides produced by the decomposition of solvent.[63]

However, SEI film formation occurs vigorously during the discharge process which looks similar to adsorption. In this regard, the changes of F 1s on the CP electrode surface were distinguish during the charge/discharge process to illustrate the sodium storage mechanism as summarized in Fig. S5b.† As one of the components of the SEI film, the Na–F bond at 684.5 eV is observed at discharge to 0.25 V for the CP electrode, showing that the SEI film starts to form around 0.25 V during the discharge process. In the meantime, according to the

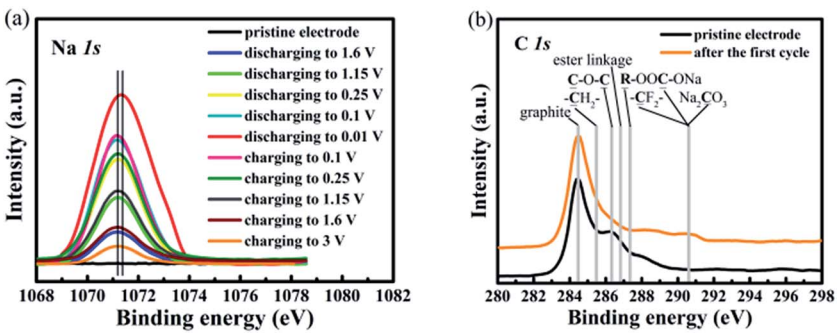

Fig. 8 (a) Na 1s XPS spectra for the CP electrodes test under different cut-off voltages and the pristine electrode. (b) C 1s XPS spectra for the CP electrode tests after the first cycle and the pristine electrode.

previous research reports, the addition of FEC favors the stable formation of the SEI film, and in combination with the CV curve analysis, the SEI film tends to be stable after the first cycle. As we know that the surface adsorption behavior appears from the initial discharge and continues in the cycles, it is further verified that the sodium storage mechanism of the CP electrode in the high potential slope region is the adsorption behavior of the material surface rather than the interference caused by the SEI film formation. Finally, the sodium storage mechanism of the CP electrode combined with the results of CV and galvanostatic charge/discharge cycling profiles can be concluded: (I) the high potential slope region corresponds to the sodium ion adsorption on the surface of the amorphous carbon materials; (II) the low potential platform region belongs to sodium ion insertion into the graphite sheets.

Conclusions

In the present work, hard carbon anode materials for SIBs have been successfully prepared using cherry petals as the raw material. When CPs were used as an anode material for SIBs, the unique structural features endow it with excellent electrochemical performance: a relatively stable capacity of 300.2 mA h g^{-1} at a current density of 20 mA g^{-1} with a quite high initial Coulomb efficiency of 67.3%. Moreover, after 500 cycles at 500 mA g^{-1}, the capacity retention is as high as 89.8% with little capacity fading.

It is observed that the superior properties of the CP electrode can be attributed to the synergistic effect associated with the flake morphology that has nanoscale mesopores, the presence of nitrogen/oxygen functional groups on the surface, and the expanded interlayer distance ($\sim$0.44 nm). These native properties promote the diffusion of the sodium ion, stabilize the formation of the SEI film, increase the partial improvement of the sodium ion stored defect sites, and enhance the storage of the sodium ion. Innovatively, the sodium ion storage behaviors of the final products have been investigated in detail by CV and XPS analysis. The obtained results demonstrate that the sodium storage in the CP can be roughly divided into two main mechanisms: the high potential slope region is the adsorption process of the sodium ion on the surface of the material, and the low potential platform region belongs to the sodium intercalation into the graphite sheets. Considering the excellent electrochemical performance and cost-effective synthesis, we believe that the CP electrode materials combined with the simple and economical preparation process and excellent electrochemical properties can be widely used in high performance SIBs and other energy storage devices.

Conflicts of interest

There are no conflicts to declare.

Acknowledgements

Financial support from the National Natural Science Foundation of China (No. 51604132 and 51764029), the Provincial Natural Science Foundation of Yunnan (No. 2017FB085) and the State Key Laboratory of Physical Chemistry of Solid Surfaces of Xiamen University (201506) is gratefully acknowledged. We also thank Yanjia Zhang and Jinmei Ji for their helpful discussions.

Notes and references

1 Y. Nishi, *J. Power Sources*, 2001, **100**, 101–106.
2 M. Armand and J. M. Tarascon, *Nature*, 2008, **451**, 652–657.
3 N. Yabuuchi, K. Kubota, M. Dahbi and S. Komaba, *Chem. Rev.*, 2014, **114**, 11636.
4 J. Y. Hwang, S. T. Myung and Y. K. Sun, *Chem. Soc. Rev.*, 2017, **46**, 3529–3614.
5 J. Liu, M. Zheng, X. Shi, H. Zeng and H. Xia, *Adv. Funct. Mater.*, 2016, **26**, 919–930.
6 Y. Zhang, X. Li, M. Zhang, S. Liao, P. Dong, J. Xiao, Y. Zhang and X. Zeng, *Ceram. Int.*, 2017, **43**, 14082–14089.
7 D. P. Divincenzo and E. J. Mele, *Phys. Rev. B*, 1985, **32**, 2538–2553.
8 P. Ge and M. Fouletier, *Solid State Ionics*, 1988, **28**, 1172–1175.
9 S. W. Kim, D. H. Seo, X. Ma, G. Ceder and K. Kang, *Adv. Energy Mater.*, 2012, **2**, 710–721.
10 H. Pan, Y. S. Hu and L. Chen, *Energy Environ. Sci.*, 2013, **6**, 2338–2360.
11 V. L. Chevrie and G. Ceder, *J. Electrochem. Soc.*, 2011, **158**, A1011–A1014.
12 R. Alcántara, F. F. Madrigal, P. Lavela, J. L. Tirado, J. J. Mateos, C. G. Salazar, R. Stoyanova and E. Zhecheva, *Carbon*, 2000, **38**, 1031–1041.
13 D. A. Stevens and J. R. Dahn, *J. Electrochem. Soc.*, 2000, **147**, 1271–1273.
14 S. Komaba, W. Murata, T. Ishikawa, N. Yabuuchi, T. Ozeki, T. Nakayama, A. Ogata, K. Gotoh and K. Fujiwara, *Adv. Funct. Mater.*, 2011, **21**, 3859–3867.
15 E. Irisarri, A. Ponrouch and M. R. Palacin, *J. Electrochem. Soc.*, 2015, **162**, 2476–2482.
16 S. Wenzel, T. Hara, J. Janek and P. Adelhelm, *Energy Environ. Sci.*, 2011, **4**, 3342–3345.
17 Y. Li, S. Xu, X. Wu, J. Yu, Y. Wang, Y. S. Hu, H. Li, L. Chen and X. Huang, *J. Mater. Chem. A*, 2014, **3**, 71–77.
18 Z. Jian, B. Zhao, P. Liu, F. Li, M. Zheng, M. Chen, Y. Shi and H. Zhou, *Chem. Commun.*, 2014, **50**, 1215–1217.
19 L. Cao, W. Hui, Z. Xu, J. Huang, P. Zheng, J. Li and Q. Sun, *J. Alloys Compd.*, 2017, **695**, 632–637.
20 K. Hong, L. Qie, R. Zeng, Z. Yi, W. Zhang, D. Wang, W. Yin, C. Wu, Q. Fan, W. Zhang and Y. Huang, *J. Mater. Chem. A*, 2014, **2**, 12733–12738.
21 H. Wang, W. Yu, J. Shi, N. Mao, S. Chen and W. Liu, *Electrochim. Acta*, 2016, **188**, 103–110.
22 E. M. Lotfabad, J. Ding, K. Cui, A. Kohandehghan, W. P. Kalisvaart, M. Hazelton and D. Mitlin, *ACS Nano*, 2014, **8**, 7115–7129.
23 L. Wu, D. Buchholz, C. Vaalma, G. A. Giffin and S. Passerini, *ChemElectroChem*, 2016, **3**, 292–298.

24 H. Li, F. Shen, W. Luo, J. Dai, X. Han, Y. Chen, Y. Yao, H. Zhu, K. Fu, E. Hitz and L. Hu, *ACS Appl. Mater. Interfaces*, 2016, **8**, 2204–2210.
25 Y. Cao, L. Xiao, M. L. Sushko, W. Wang, B. Schwenzer, J. Xiao, Z. Nie, L. V. Saraf, Z. Yang and J. Liu, *Nano Lett.*, 2012, **12**, 3783–3787.
26 X. Meng, P. E. Savage and D. Deng, *Environ. Sci. Technol.*, 2015, **49**, 12543–12550.
27 Y. Wen, K. He, Y. Zhu, F. Han, Y. Xu, I. Matsuda, Y. Ishii, J. Cumings and C. Wang, *Nat. Commun.*, 2014, **5**, 4033.
28 J. R. Dahn, W. Xing and Y. Gao, *Carbon*, 1997, **35**, 825–830.
29 Y. Liu, N. Zhang, C. Yu, L. Jiao and J. Chen, *Nano Lett.*, 2016, **16**, 3321–3328.
30 Y. Liu, N. Zhang, L. Jiao and J. Chen, *Adv. Mater.*, 2015, **27**, 6702–6707.
31 S. Qiu, L. Xiao, M. L. Sushko, K. S. Han, Y. Shao, M. Yan, X. Liang, L. Mai, J. Feng, Y. Cao, X. Ai, H. Yang and J. Liu, *Adv. Energy Mater.*, 2017, **7**, 1700403.
32 P. Ge and M. Fouletier, *Solid State Ionics*, 1988, **28–30**, 1172–1175.
33 D. Yang, A. Velamakanni, G. Bozoklu, S. Park, M. Stoller, R. D. Piner, S. Stankovich, I. Jung, D. A. Field, C. A. Ventrice Jr and R. S. Ruoffa, *Carbon*, 2009, **47**, 145–152.
34 H. R. Byon, B. M. Gallant, S. W. Lee and S. H. Yang, *Adv. Funct. Mater.*, 2013, **23**, 1037–1045.
35 L. Tang, Y. Wang, Y. Li, H. Feng, J. Lu and J. Li, *Adv. Funct. Mater.*, 2009, **19**, 2782–2789.
36 J. Ou, L. Yang, Z. Zhang and X. Xi, *Microporous Mesoporous Mater.*, 2017, **237**, 23–30.
37 Y. Matsumura, S. Wang and J. Mondori, *J. Electrochem. Soc.*, 1995, **142**, 2914.
38 M. Arakawa and J. I. Yamaki, *J. Electroanal. Chem.*, 1987, **219**, 273.
39 J. Li, V. Mauricea, J. Mrowiecka, A. Seyeux, S. Zanna, L. Klein, S. Sun and P. Marcusa, *Electrochim. Acta*, 2009, **54**, 3700.
40 K. Tang, L. Fu, R. J. White, L. Yu, M. M. Titirici, M. Antonietti and J. Maier, *Adv. Energy Mater.*, 2012, **2**, 873–877.
41 H. Hou, C. E. Banks, M. Jing, Y. Zhang and X. Ji, *Adv. Mater.*, 2015, **27**, 7861–7866.
42 W. Luo, C. Bommier, Z. Jian, X. Li, R. Carter, S. Vail, Y. Lu, J. J. Lee and X. Ji, *ACS Appl. Mater. Interfaces*, 2015, **7**, 2626–2631.
43 S. J. R. Prabakar, J. Jeong and M. Pyo, *Electrochim. Acta*, 2015, **161**, 23–31.
44 T. Chen, Y. Liu, L. Pan, T. Lu, Y. Yao, Z. Sun, D. H. C. Chua and Q. Chen, *J. Mater. Chem. A*, 2014, **2**, 4117–4121.
45 X. Zhou and Y. G. Guo, *ChemElectroChem*, 2014, **1**, 83–86.
46 Y. Li, L. Mu, Y. S. Hu, H. Li, L. Chen and X. Huang, *Energy Storage Materials*, 2016, **2**, 139–145.
47 X. Zhou, X. Zhu, X. Liu, Y. Xu, Y. Liu, Z. Dai and J. Bao, *J. Phys. Chem. C*, 2014, **118**, 22426–22431.
48 J. Jin, B. Yu, Z. Shi, C. Wang and C. Chong, *J. Power Sources*, 2014, **272**, 800–807.
49 Y. X. Wang, S. L. Chou, H. K. Liu and S. X. Dou, *Carbon*, 2013, **57**, 202–208.
50 K. Tang, L. Fu, R. J. White, L. Yu, M. M. Titirici, M. Antonietti and J. Maier, *Adv. Energy Mater.*, 2012, **2**, 873–877.
51 Z. Wang, L. Qie, L. Yuan, W. Zhang, X. Hu and Y. Huang, *Carbon*, 2013, **55**, 328–334.
52 X. Wang, G. Li, F. M. Hassan, J. Li, X. Fan, R. Batmaz, X. Xiao and Z. Chen, *Nano Energy*, 2015, **15**, 746–754.
53 X. F. Luo, C. H. Yang, Y. Y. Peng, N. W. Pu, M. D. Ger, C. T. Hsieh and J. K. Chang, *J. Mater. Chem. A*, 2015, **3**, 10320–10326.
54 H. Song, N. Li, H. Cui and C. Wang, *Nano Energy*, 2014, **4**, 81–87.
55 H. Liu, M. Jia, N. Sun, B. Cao, R. Chen, Q. Zhu, F. Wu, N. Qiao and B. Xu, *ACS Appl. Mater. Interfaces*, 2015, **7**, 27124–27130.
56 Q. C. Zhuang, X. Y. Qiu, S. D. Xu, Y. H. Qiang and S. G. Sun, *Progr. Chem.*, 2010, **22**, 1044–1057.
57 V. Augustyn, J. Come, M. A. Lowe, J. W. Kim, P. L. Taberna, S. H. Tolbert, H. D. Abruña, P. Simon and B. Dunn, *Nat. Mater.*, 2013, **12**, 518–522.
58 J. Wang, J. Polleux, J. Lim and B. Dunn, *J. Phys. Chem. C*, 2007, **111**, 14925–14931.
59 Y. Li, Y. S. Hu, M. M. Titirici, L. Chen and X. Huang, *Adv. Energy Mater.*, 2016, **6**, 1600659.
60 F. A. Soto, P. Yan, M. H. Engelhard, A. Marzouk, C. Wang, G. Xu, Z. Chen, K. Amine, J. Liu, V. L. Sprenkle, F. E. Mellouhi, P. B. Balbuena and X. Li, *Adv. Mater.*, 2017, **29**, 1606860.
61 S. Komaba, T. Ishikawa, N. Yabuuchi, W. Murata, A. Ito and Y. Ohsawa, *ACS Appl. Mater. Interfaces*, 2011, **3**, 4165–4168.
62 L. Ji, M. Gu, Y. Shao, X. Li, M. H. Engelhard, B. W. Arey, W. Wang, Z. Nie, J. Xiao, C. Wang, J. G. Zhang and J. Liu, *Adv. Mater.*, 2014, **26**, 2901–2908.
63 S. Komaba, W. Murata, T. Ishikawa, N. Yabuuchi, T. Ozeki, T. Nakayama, A. Ogata, K. Gotoh and K. Fujiwara, *Adv. Funct. Mater.*, 2011, **21**, 3859–3867.

